Article ID: 1006-8775(2011) 03-0231-16

A STUDY OF PARTITIONING *Q* VECTOR ON BACKGROUND CONDITIONS OF A TORRENTIAL RAINFALL OVER SHANGHAI, CHINA ON 25 AUGUST 2008

YUE Cai-jun (岳彩军)[1, 2], LU Xiao-qin (鲁小琴)[1, 2], Xiaofan LI (李小凡)[3], ZONG Zhi-ping (宗志平)[4]

(1. Shanghai Typhoon Institute of the China Meteorological Administration, Shanghai 200030 China; 2. Laboratory of Typhoon Forecast Technique/CMA, Shanghai 200030 China; 3. Joint Center for Satellite Data Assimilation and NOAA/NESDIS/Center for Satellite Applications and Research, Camp Springs, Maryland, USA; 4. National Meteorological Center of CMA, Beijing 100081 China)

Abstract: A rainfall that occurred during 0200–1400 Beijing Standard Time (BST) 25 August 2008 shows the rapid development of a convective system, a short life span, and a record rate of 117.5 mm h^{-1} for Xujiahui station since 1872. To study this torrential rainfall process, the partitioning method of ***Q*** vector is developed, in which a moist ***Q*** vector is first separated into a dry ageostrophic ***Q*** vector ($\boldsymbol{Q}^D$) and a diabatic-heating component. The dry ageostrophic ***Q*** vector is further partitioned along isothermal lines in the natural coordinate to identify different scale forcing in adiabatic atmosphere, and the large-scale and convective condensational heating in non-uniform saturated atmosphere, convective condensational heating, and Laplace of diabatic heating that includes radiative heating and other heating and cooling processes, are calculated to study the forcing from diabatic heating. The effects of the environmental conditions on the development of the rainfall processes are diagnosed by performing the partitioning of ***Q*** vector based on 6-hourly NCEP/NCAR Final Analysis (FNL) data with the horizontal resolution of $1° \times 1°$. The results include the following: (1) a low-pressure inverted trough associated with the landfall of Typhoon Nuri (2008), a strong southwesterly jet along the western side of the subtropical high, and an eastward-propagating westerly low-pressure trough provide favorable synoptic conditions for the development of torrential rainfall; (2) the analysis of $\boldsymbol{Q}^D$ vector showed that the upward motions forced by the convergence of $\boldsymbol{Q}^D$ vector in the lower troposphere (1000–600 hPa) favor the development of torrential rainfall. When $\boldsymbol{Q}^D$ vector converges in the upper troposphere (500–100 hPa), upward motions in the whole air column intensify significantly to accelerate the development of torrential rainfall; (3) the partitioning analysis of $\boldsymbol{Q}^D$ vector reveals that large-scale forcing persistently favors the development of torrential rainfall whereas the mesoscale forcing speeds up the torrential rainfall; (4) the calculations of large-scale condensational heating in non-uniform saturated atmosphere, convective condensational heating, and Laplace of diabatic heating showed that the forcing related to diabatic heating has the positive feedback on the convective development, and such positive feedback decays and dissipates when the convective system propagates eastward and weakens.

Key words: background conditions of torrential rainfall; partitioning of ***Q*** vector; dry ageostrophic ***Q*** vector; diabatic heating

CLC number: P435 **Document code:** A **doi:** 10.3969/j.issn.1006-8775.2011.03.005

1 INTRODUCTION

The forecast of torrential rainfall is an important, difficult task of weather forecasting, in particular, the forecast of torrential rainfall with rapid development of a convective system during a short life span has been barely improved. With a rapid development of Chinese economy, the direct and indirect economic

Received 2009-11-24; **Revised** 2010-05-07; **Accepted** 2011-07-15

Foundation item: National Natural Science Foundation of China (40875025, 40875030, 40775033, 40921160381), Shanghai Natural Science Foundation of China (08ZR1422900), Key Promotion Project of New Meteorology Technology of the China Meteorological Administration in 2009 (09A13)

Biography: YUE Cai-jun, assistant professor, Ph.D., mainly undertaking the research on mesoscale dynamics and ocean-atmosphere interaction.

Corresponding author: YUE Cai-jun, e-mail: yuecaijun2000@163.com

losses associated with torrential rainfall becomes more and more problematic, especially, in the developed and densely populated modern metropolitan areas. On 25 August 2008, a torrential rainfall event occurred over Shanghai, China, which led to a significant flood over a large area, a severe traffic jam, and a big economic loss[1]. Thus, the improvement of rainfall forecasting skill is one of the most urgent tasks needed to be solved by operational weather communities. Meanwhile, the improvement of rainfall forecast relies on, with in-depth studies, better understanding of development of torrential rainfall. It is well known that torrential rainfall is always forced by upward motions associated with favorable large-scale synoptic conditions. The analysis of upward motions, which cannot be directly measured, relies on the improvement of diagnostic tools. As an advanced tool for diagnosing upward motions associated with rainfall, $\boldsymbol{Q}$ vector has been studied and applied to the diagnosis of various weather systems[2-4] since it was introduced by Hoskins et al.[5] The $\boldsymbol{Q}$ vector can be categorized into dry and moist $\boldsymbol{Q}$ vectors. The dry $\boldsymbol{Q}$ vector does not include atmospheric diabatic heating, such as geostrophic $\boldsymbol{Q}$ vector[5], semi-geostrophic $\boldsymbol{Q}$ vector[6], generalized $\boldsymbol{Q}$ vector[7], $\boldsymbol{C}$ vector[8], generalized $\boldsymbol{C}$ vector[9], dry ageostrophic $\boldsymbol{Q}$ vector ($\boldsymbol{Q}^D$)[10] and modified dry ageostrophic $\boldsymbol{Q}$ vector[11, 12]. The moist $\boldsymbol{Q}$ vector contains such atmospheric diabatic heating terms as moist ageostrophic $\boldsymbol{Q}$ vector (moist $\boldsymbol{Q}$ vector)[13-16], modified moist ageostrophic $\boldsymbol{Q}$ vector (modified moist $\boldsymbol{Q}$ vector)[17-19], and moist $\boldsymbol{Q}$ vector in non-uniform saturated atmosphere[20, 21]. Previous studies[11, 12, 22-44] revealed that the partitioning of $\boldsymbol{Q}$ vector, a very useful diagnostic tool, can provide valuable diagnosis of weather systems. The partitioning of dry $\boldsymbol{Q}$ vector is mainly done along isothermal lines in the natural coordinate[22-33], along iso-height lines in the natural coordinate[11, 12, 34, 35], parallel to isothermal lines into geostrophic vorticity and deformation component[36], and with partitioned wind field retrieved from potential vorticity[37]. The partitioning of moist $\boldsymbol{Q}$ vector is mainly accomplished along isothermal lines in the natural coordinate[38-42], and the addition of components of condensational heating and $\boldsymbol{Q}^D$ vector at different scales[43], with direct partition done to the components of dry ageostrophic $\boldsymbol{Q}$ vector and diabatic heating[44]. The aforementioned partitioning methods show that the $\boldsymbol{Q}$ vector and associated partitioned components have similar diagnostic features. Different partitioning methods can be applied to the diagnosis of development of weather systems associated with torrential rainfall. Among them, the partitioning of $\boldsymbol{Q}$ vector along isothermal lines in the natural coordinate is the most popular technique. Yue et al.[38, 39] conducted the partitioning of moist ageostrophic $\boldsymbol{Q}$ vector and modified moist ageostrophic $\boldsymbol{Q}$ vector to study Meiyu torrential rainfall events over the area between the middle and lower reaches of the Yangtze and the Huaihe River in 1991 and found that the partitioning of $\boldsymbol{Q}$ vector results in meaningful scale separation of vertical velocity for better evaluation of potential physical mechanisms associated with the development of Meiyu torrential rainfall. Wang et al.[40] carried out similar partitioning of moist ageostrophic $\boldsymbol{Q}$ vector along isothermal lines in the natural coordinate and revealed the mesoscale features of unusual torrential rainfall events that occurred over Sichuan-Shanxi area along the east side of Tibetan Plateau. Yang et al.[41] also performed similar partitioning to analyze unusual torrential rainfall that occurred in Shandong province during the spring and fall and showed that the convergence of moist $\boldsymbol{Q}$ vector vertical to the isothermal lines is similar to the convergence of moist $\boldsymbol{Q}$ vector in a spring torrential rainfall case during 17–18 April 2003, when mesoscale upward motions were dominant. In contrast, the convergence of moist $\boldsymbol{Q}$ vector component parallel to the isothermal lines is similar to the convergence of moist $\boldsymbol{Q}$ vector in a fall torrential rainfall case during 10–12 October 2003, in which the large-scale upward motions of the torrential rainfall is mainly of large scale mixed with embedded meso- and fine-scale upward motions and precipitation is of a mixed pattern. Liang et al.[42] separated the moist $\boldsymbol{Q}$ vector into components vertical and parallel to isothermal lines and found that mesoscale upward motions and convective rainfall dominated during torrential rainfall whereas the convergence of $\boldsymbol{Q}$ vector component parallel to the isothermal lines became larger after the torrential rainfall. Unlike Yue et al.[39] and Liang[42], Yue[43] first separated dry ageostrophic $\boldsymbol{Q}$ vector along isothermal lines in the natural coordinate to derive $\boldsymbol{Q}_s^D$ and $\boldsymbol{Q}_n^D$ and then combined them, respectively, with large-scale and convective condensational heating in the analysis of Typhoon Haitang (2005). Long et al.[44] partitioned the moist $\boldsymbol{Q}$ vector into dynamic and diabatic components and applied its analysis to three heavy rainfall events. In fact, this research work is to separate the moist $\boldsymbol{Q}$ vector into the forcing from dry ageostrophic $\boldsymbol{Q}$ vector and diabatic heating. The aforementioned studies demonstrated that the partitioning of $\boldsymbol{Q}$ vector is an efficient tool for studying torrential rainfall processes. The advantage of analyzing moist $\boldsymbol{Q}$ vector is the inclusion of diabatic heating. Recently, Yang et al.[20] and Gao[21] proposed a method of separating condensational heating from other diabatic heating (including radiative heating and other heating/cooling) in the analysis of moist $\boldsymbol{Q}$ vector in non-uniform saturated atmosphere. In this study, a new technique of

partitioning ***Q*** vector is suggested, which calculates the dry ageostrophic ***Q*** vector and associated separation, the forcing from large-scale condensational heating in non-uniform saturated atmosphere, convective condensational heating, and diabatic heating that includes radiative heating and other heating/cooling. The backgrounds associated with torrential rainfall over Shanghai, China on 25 August 2008 as calculated from 6-hourly NCEP/NCAR Final Analysis (FNL) data with horizontal resolution of 1° ×1° are presented in the next section. The partitioning of ***Q*** vector is performed in section 3 and associated results are analyzed and discussed in section 4. A conclusion is given in section 5.

2 TORRENTIAL RAINFALL EVENT

2.1 *Characteristics of precipitation*

Figure 1a shows the torrential rainfall over the southern areas of Jiangsu and Anhui Provinces and moderate and heavy rainfall over the central and northern areas of Zhejiang Province and heavy rainfall in most parts of Shanghai area (referred to as "the area" hereafter) during 2000 Beijing Standard time (BST) 24 August to 2000 BST 25 August 2008. Precipitation did not occur in the area from 2000 BST 24 August to 0000 BST 25 August. The weak rainfall occurred during 0100-0500 BST 25 August. A moderate rainfall with an area-mean rain rate of 1.8 mm h^{-1} appeared over the western suburbs of Shanghai. Then, the rainfall rapidly intensified and its area-mean rain rate increased from 9.2 mm h^{-1} at 0700 BST 25 August to 16.8 mm h^{-1} at 0800 BST 25 August. The rainfall significantly weakened at 0900 BST and dissipated at 1400 BST 25 August (Fig. 1b). Seven automatic raingauge stations showed rain rates of more than 100 mm over a 12-h period, and in particular, Xujiahui station showed 117.5 mm h^{-1} (Fig. 1c), which sets a historical record since 1872. The rainfall case features a short lifespan and large area-mean rainfall.

2.2 *Evolution of brightness temperature (TBB)*

The analysis of horizontal distributions of TBB using the IR1 data with a resolution of 0.05° × 0.05°, measured by the geostationary satellite MT1R, shows that the precipitating clouds with cloud-top temperatures lower than -30° C occurred partially over the area at 0200 BST 25 August (Fig. 2). The clouds extended to western suburbs at 0600 BST, merged over the central and northern parts of the area and grew significantly at 0700 BST, with cloud-top temperatures lower than -50° C. They then continued to intensify while slowly propagating eastward. The clouds completely moved into the East China Sea at 1100 BST. The cloud-top temperature over the area warmed up to -30° C and continued to increase at 1400 BST while the precipitating cloud systems further weakened and dissipated.

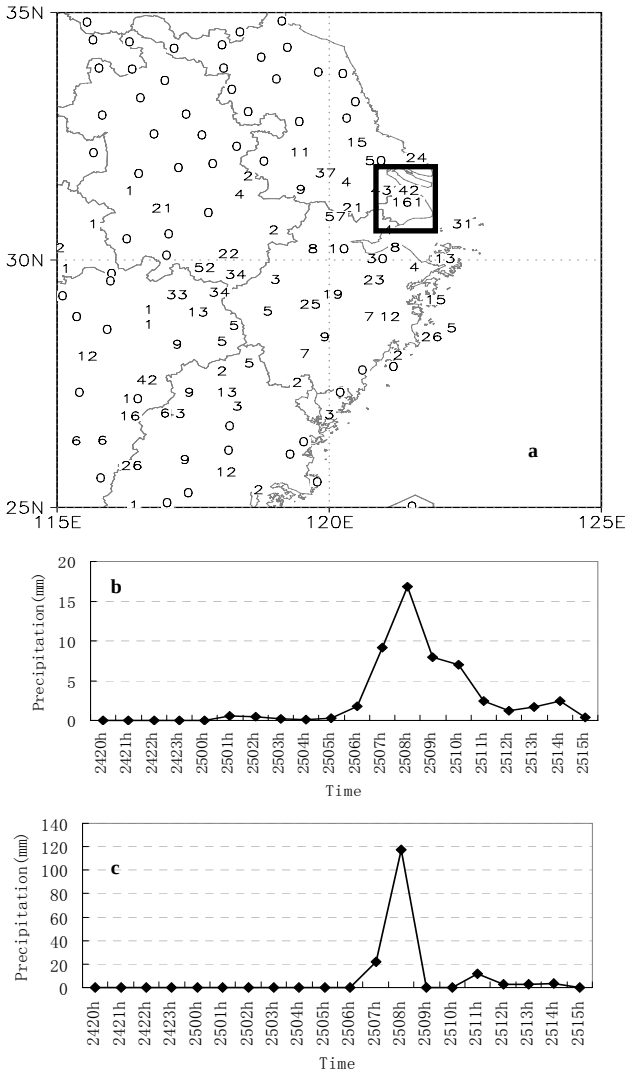

Fig. 1. a: Observed 24-h cumulative rainfall amount during 2000 BST 24 August to 2000 BST 25 August 2008 (Shanghai is marked by 口); b: hourly mean rain amount over automatic raingauge stations over the area; c: hourly rain amount over Xujiahui station. Unit: mm

2.3 *Synoptic background*

The development of the torrential rainfall is much affected by three surrounding weather systems: a low-pressure inverted trough associated with the landfall of Typhoon Nuri (2008), a strong southwesterly jet along the western side of the subtropical high, and an eastward-propagating westerly low-pressure trough. The three systems worked together to provide favorable conditions for the formation and development of the torrential rainfall. An 850-hPa synoptic chart shows that moisture converged over the area at 2000 BST 24 August (Fig. 3). The relative humidity was larger than

80% before 1400 BST 25 August. A cut-off low pressure, formed over the middle and lower ranches of the Yangtze River, was located over southern Anhui Province at 0200 BST 25 August, propagated eastward to the area, and moved into the East China Sea at 1400 BST. The synoptic patterns at 700 hPa (not shown) are similar to those at 850 hPa. A 500-hPa synoptic chart reveals that a westerly low-pressure trough formed upstream of the area west of 115° E at 2000 BST 24 August (Fig. 4). It moved to 116° E at 0200 BST 25 August, and continued to propagate eastward to the area. Finally, it moved into the sea at 1400 BST 25 August. The moisture increased around 0200 BST 25 August, and the relative humidity was over 80%, with the water vapor, associated with an eastward-propagating low-pressure trough, merging with the moist regions at the northern side of the subtropical high. Thus, large-scale circulations provide favorable conditions for both water vapor and dynamic lifting.

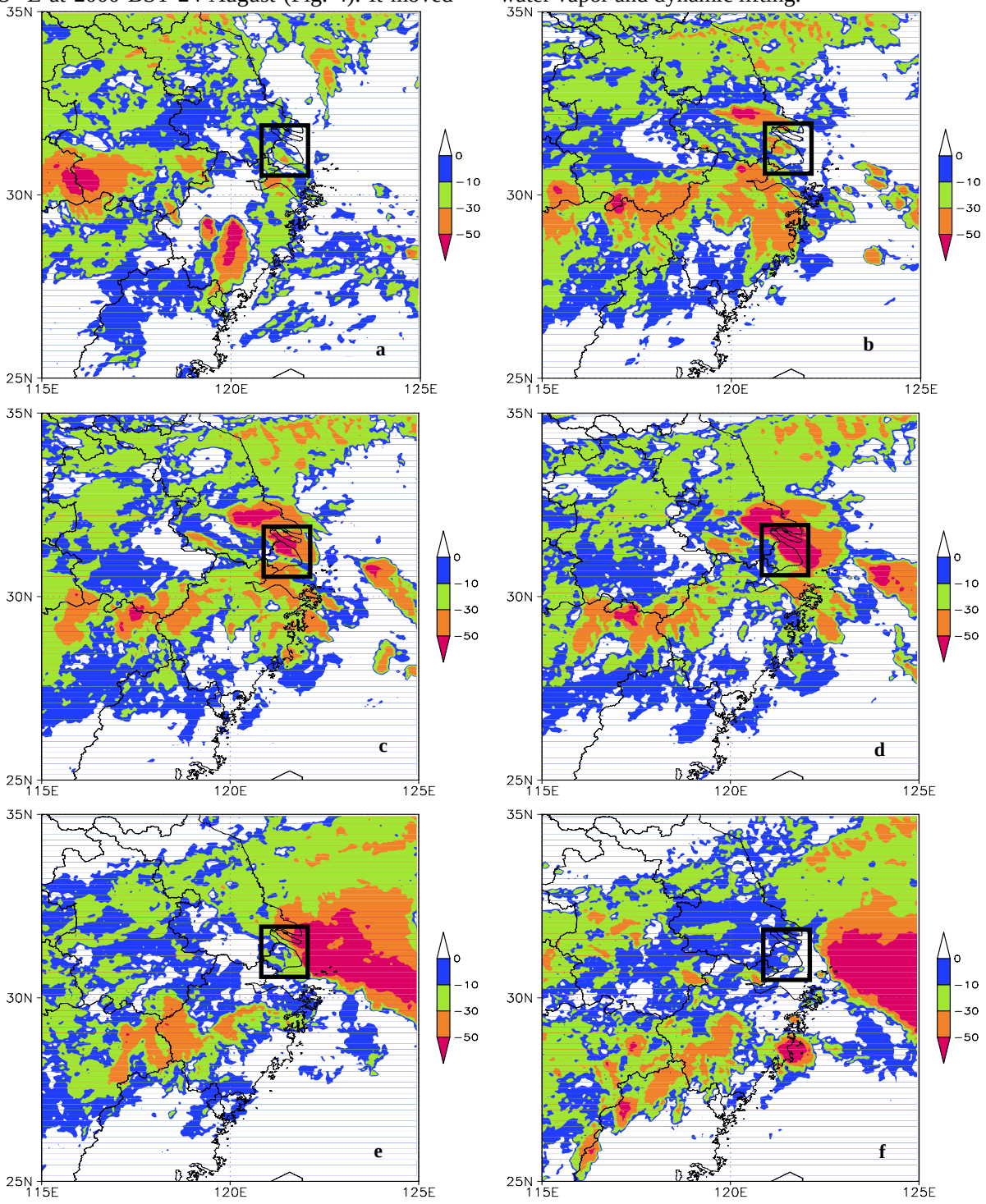

Fig. 2. Horizontal distributions of brightness temperature (°C) using IR1 data measured by the geostationary satellite MT1R at (a) 0200 BST, (b) 0600 BST, (c) 0700 BST, (d) 0800 BST, (e) 1100 BST, and (f) 1400 BST 25 August 2008. Shanghai is marked by □.

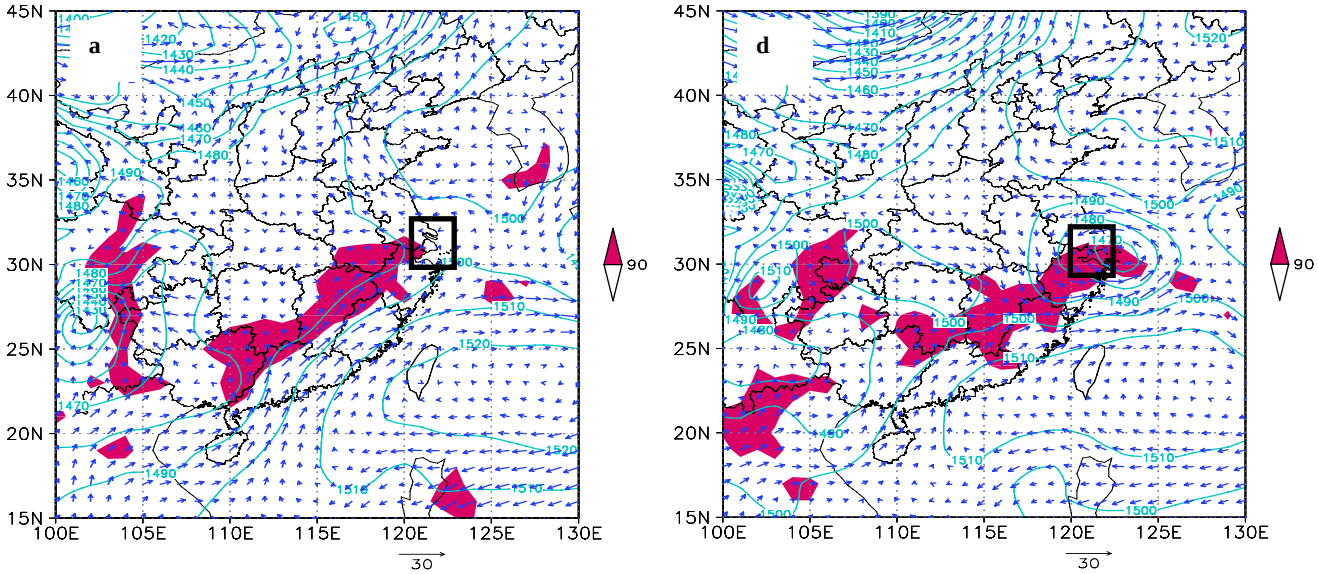

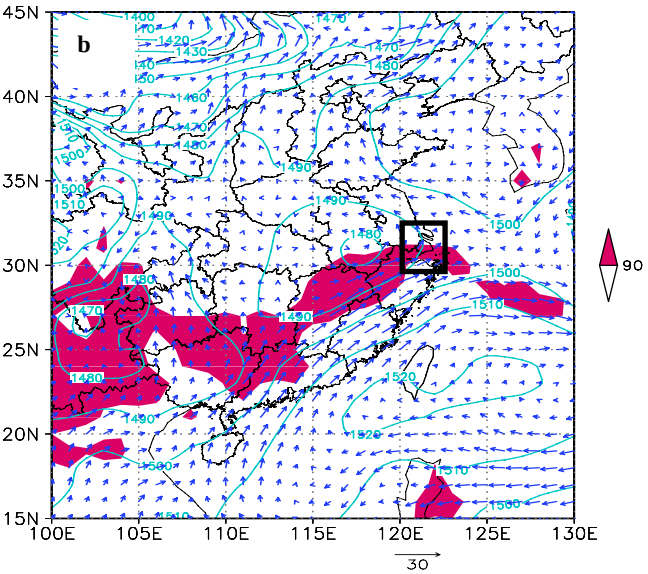

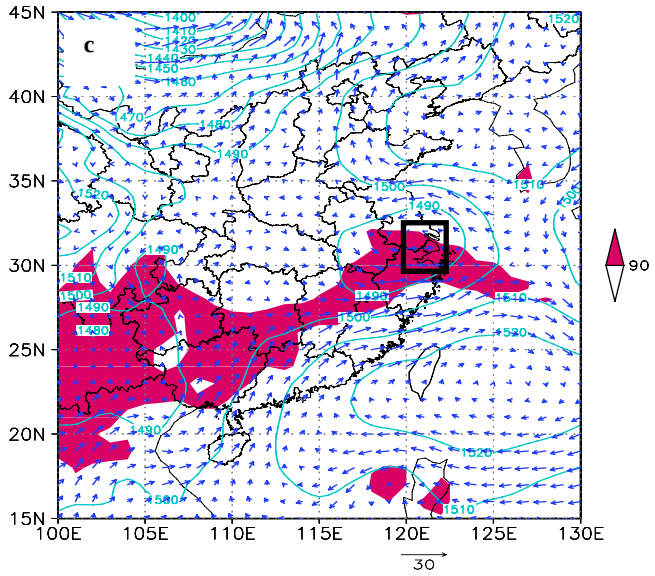

Fig. 3. 850-hPa synoptic charts at (a) 2000 BST 24 August, (b) 0200 BST 25 August, (c) 0800 BST, and (d) 1400 BST 25 August. The contours denote the geopotential height at intervals of 10 gpm. The arrows are for the winds (m s^{-1}). The relative humidity of more than 90% is shaded. Shanghai is marked by 口.

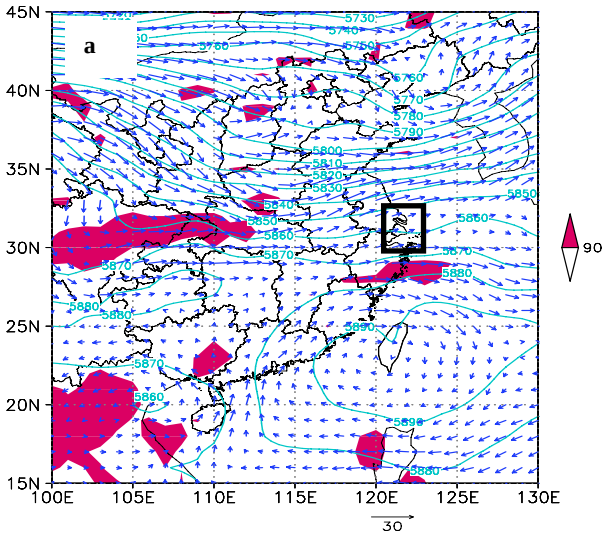

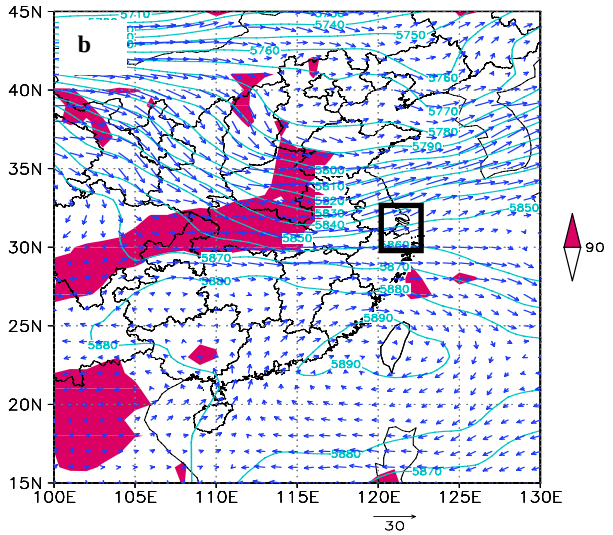

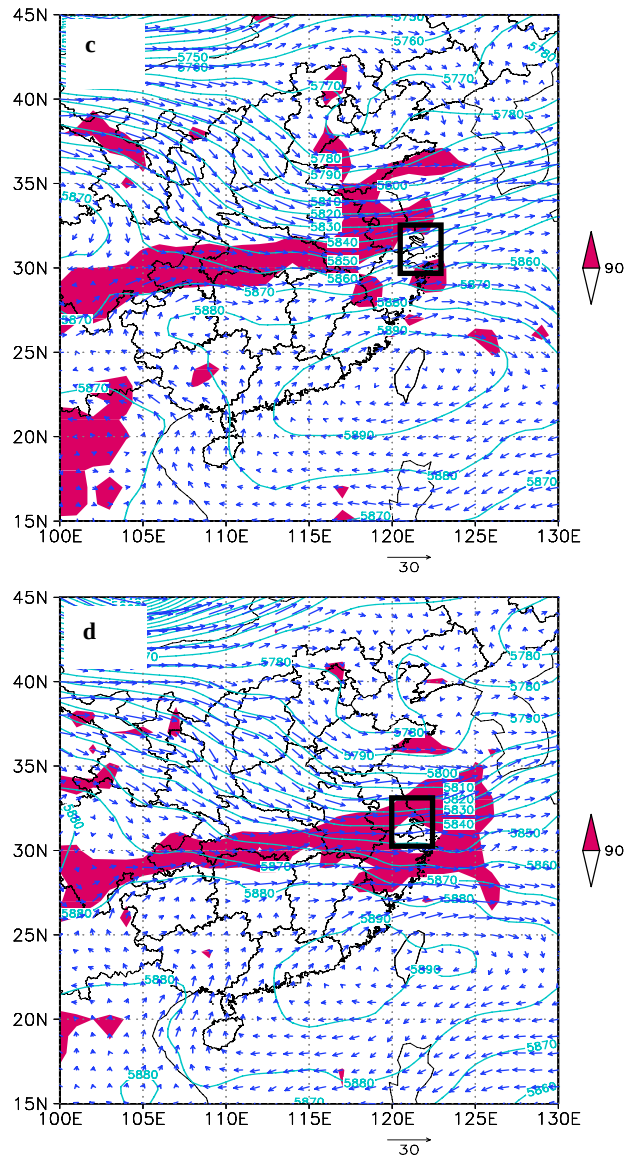

Fig. 4. As in Fig. 3 except at 500 hPa.

2.4 *Data*

NCEP/NCAR FNL data with a temporal resolution of 6 hours and a horizontal resolution of 1° ×1° are analyzed. The data contain 21 vertical levels (of 1000 hPa, 975 hPa, 950 hPa, 925 hPa, 900 hPa, 850 hPa, 800 hPa, 750 hPa, 700 hPa, 650 hPa, 600 hPa, 550 hPa, 500 hPa, 450 hPa, 400 hPa, 350 hPa, 300 hPa, 250 hPa, 200 hPa, 150 hPa, and 100 hPa). The entire air column is denoted by the average from 1000 to 100 hPa. The lower and upper atmosphere are denoted by the averages from 1000 to 600 hPa and from 500 to 100 hPa, respectively. The calculations are mainly carried out from 2000 BST 24 August to 1400 BST 25 August 2008, and the horizontal resolution of the calculated data is 1.11×10^2 km.

3 ANALYSIS OF PARTITIONING OF *Q* VECTOR

3.1 *Analysis of dry ageostrophic* ***Q*** *vector*

3.1.1 WHOLE VECTOR ANALYSIS

To examine dynamic and thermodynamic forcing associated with the development of the torrential rainfall under adiabatic conditions, the dry ageostrophic $\boldsymbol{Q}$ vector will be analyzed. Following Zhang[10], the dry ageostrophic $\boldsymbol{Q}$ vector in static, adiabatic, and frictionless atmosphere on the *f*-plane in the *p*-coordinate can be expressed by

$$\boldsymbol{Q}_x^D=\frac{1}{2}[f(\frac{\partial v}{\partial p}\frac{\partial u}{\partial x}-\frac{\partial u}{\partial p}\frac{\partial v}{\partial x})-h\frac{\partial \boldsymbol{V}}{\partial x}\cdot\nabla\theta], \quad (1)$$

$$\boldsymbol{Q}_y^D=\frac{1}{2}[f(\frac{\partial v}{\partial p}\frac{\partial u}{\partial y}-\frac{\partial u}{\partial p}\frac{\partial v}{\partial y})-h\frac{\partial \boldsymbol{V}}{\partial y}\cdot\nabla\theta], \quad (2)$$

where $h=\frac{R}{p}(\frac{p}{1000})^{R_d/C_P}$, $\theta=T(\frac{1000}{p})^{R_d/C_P}$, $\boldsymbol{V}=u\boldsymbol{i}+v\boldsymbol{j}$, and the others are conventional meteorological variables and parameters.

An ageostrophic ω equation with the forcing of divergence of $\boldsymbol{Q}^D$ vector is

$$\nabla^2(\sigma\omega)+f^2\frac{\partial^2\omega}{\partial p^2}=-2\nabla\cdot\boldsymbol{Q}^D \quad (3)$$

When ω has a wave-like solution, Eq. (3) becomes

$$\nabla\cdot\boldsymbol{Q}^D\propto\omega. \quad (4)$$

where $\omega<0$ (upward motions) as $\nabla\cdot\boldsymbol{Q}^D<0$ and $\omega>0$ (downward motions) as $\nabla\cdot\boldsymbol{Q}^D>0$.

In the lower troposphere, the convergence of $\boldsymbol{Q}^D$ vector was located over the area at 2000 BST 24 August (Fig. 5). It intensified to $-0.5\times10^{-15}\,\mathrm{hPa^{-1}\cdot s^{-3}}$ over western Shanghai at 0200 BST 25 August. At 0800 BST 25 August, the center of convergence moved to the sea northeast of Shanghai while the convergence covered most of the area. The divergence of $\boldsymbol{Q}^D$ vector occurred at 1400 BST 25 August. This indicates that the convergence of $\boldsymbol{Q}^D$ vector was located over the area from 2000 BST 24 August to 1400 BST 25 August.

In the upper troposphere, the divergence of $\boldsymbol{Q}^D$ vector was located over most of the area at 2000 BST 24 August (Fig. 6). Meanwhile, a band-shaped convergence zone of $\boldsymbol{Q}^D$ vector appeared over the northern area next to Shanghai. The convergence propagated eastward, extended southward and merged into the convergence zone over the southern part of middle- and lower-reaches of the Yangtze River while it showed a distribution of northeast-southwest orientation at 0200 BST 25 August. The convergence covered the area. At 0800 BST 25 August, the

convergence belt of $\boldsymbol{Q}^D$ vector was broken and propagated eastward to the sea. The divergence completely occupied the area at 1400 BST.

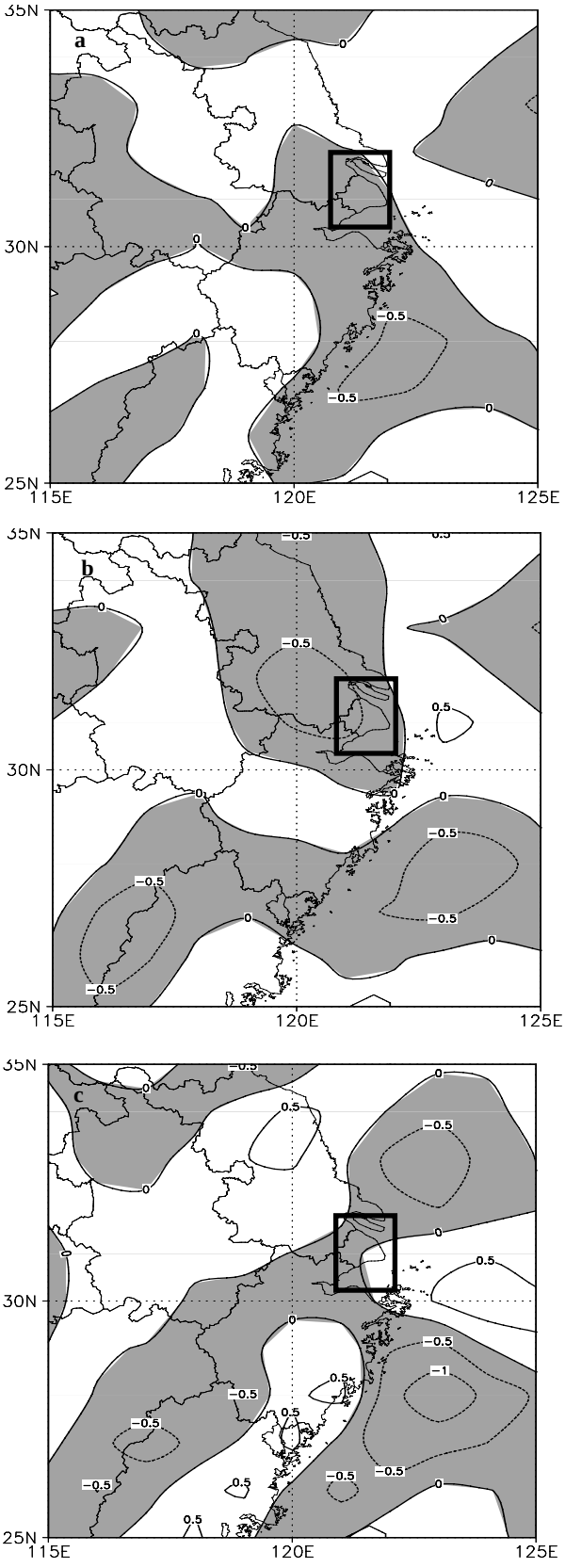

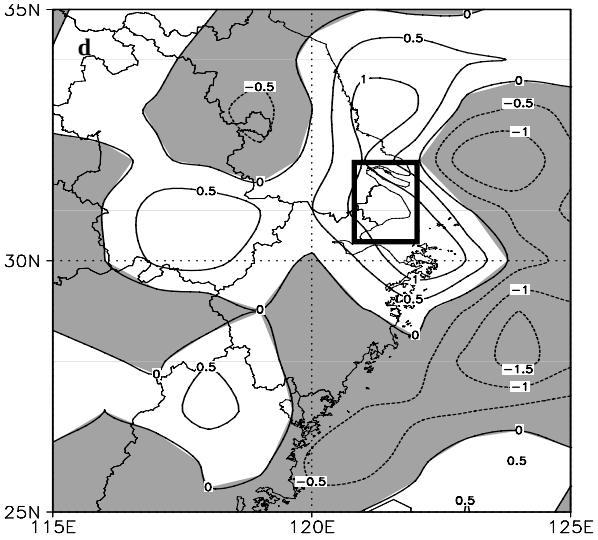

Fig. 5. $2\nabla\cdot\boldsymbol{Q}^D$ averaged in air column from 1000–600 hPa at (a) 2000 BST 24 August, (b) 0200 BST 25 August, (c) 0800 BST 25 August, and (d) 1400 BST 25 August. The contour interval is 0.5×10^{-15} hPa$^{-1}\cdot$s^{-3}, and the convergence of $2\nabla\cdot\boldsymbol{Q}^D$ is shaded. Shanghai is marked by 口.

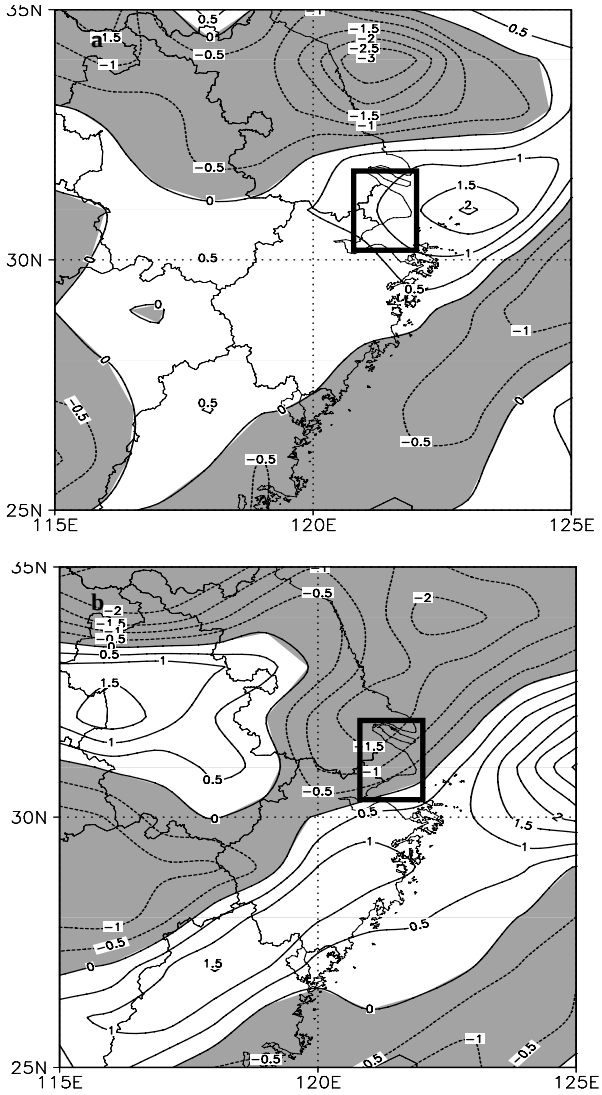

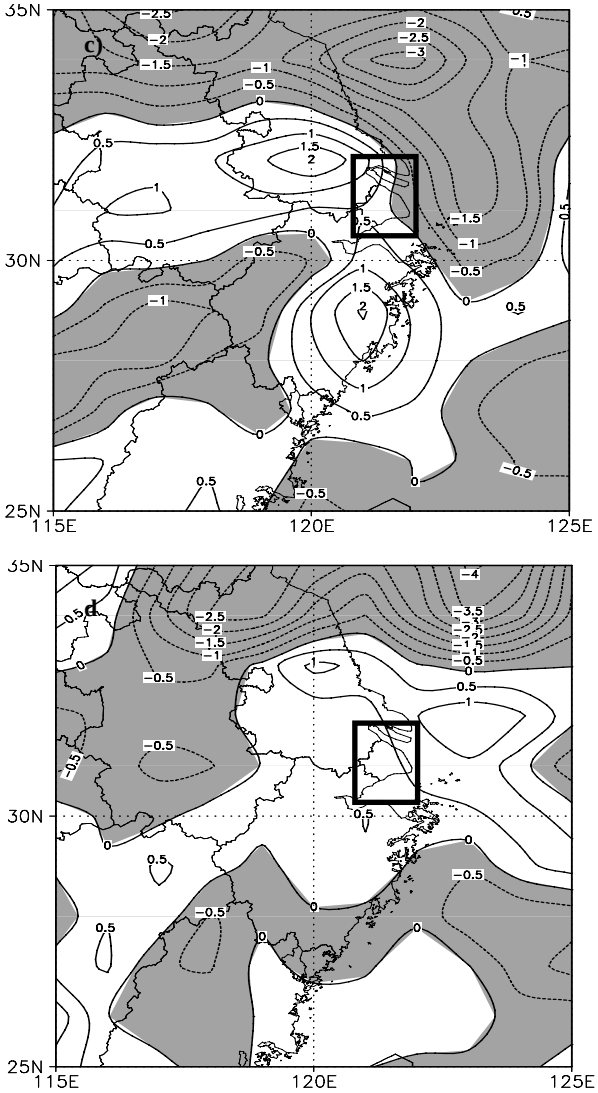

Fig. 6. As in Fig. 5 except that $2\nabla\cdot\boldsymbol{Q}^D$ is averaged in air column from 500–100 hPa

The analysis of both upper and lower troposphere shows that the convergence of $2\nabla\cdot\boldsymbol{Q}^D$ occurred in the lower troposphere whereas the divergence appeared in the upper troposphere at 2000 BST 24 August. Both the lower and upper troposphere has the convergence at 0200 BST 25 August while the convergence in the lower troposphere significantly intensified and the centers of convergence in the lower and upper troposphere were collocated. At 0800 BST, while the convergence was maintained in the lower troposphere over most of the area, the corresponding upper troposphere became divergent. The centers of convergence in the lower and upper troposphere were not collocated, indicating the weakening of the convergence. At 1400 BST, the divergence occurred in both the lower and upper troposphere. Figs. 1b, 5 and 6 reveal that the evolution of divergence of $\boldsymbol{Q}^D$ vector can be served as a precursor for the development of the torrential rainfall. The rapid intensification of the convergence of $2\nabla\cdot\boldsymbol{Q}^D$ from 2000 BST 24 August to 0200 BST 25 August predicts the torrential rainfall. The rapid weakening of the convergence of $2\nabla\cdot\boldsymbol{Q}^D$ from 0200 BST to 0800 BST 25 August indicates the suppression of rainfall. Thus, the rainfall peak occurs during this period. $2\nabla\cdot\boldsymbol{Q}^D$ turns to be divergent, indicating the dissipation of rainfall at 1400 BST 25 August. It is also noted that the convergence of $2\nabla\cdot\boldsymbol{Q}^D$ is much stronger in the upper troposphere than in the lower troposphere. With the strong convergence appearing in the upper troposphere, the convergence suddenly strengthened at 0200 BST 25 August.

3.1.2 VECTOR PARTITIONING ANALYSIS

The dry ageostrophic $\boldsymbol{Q}$ vector is partitioned along isothermal lines in the natural coordinate to obtain two components, $\boldsymbol{Q}_s^D$ and $\boldsymbol{Q}_n^D$ (Fig. 7). $\boldsymbol{Q}_s^D$ is along the isothermal direction, i.e., the direction of thermal winds, which are large-scale geostrophic. $\boldsymbol{Q}_n^D$ crosses the isothermal direction, which is mesoscale ageostrophic[22-33, 38-43].

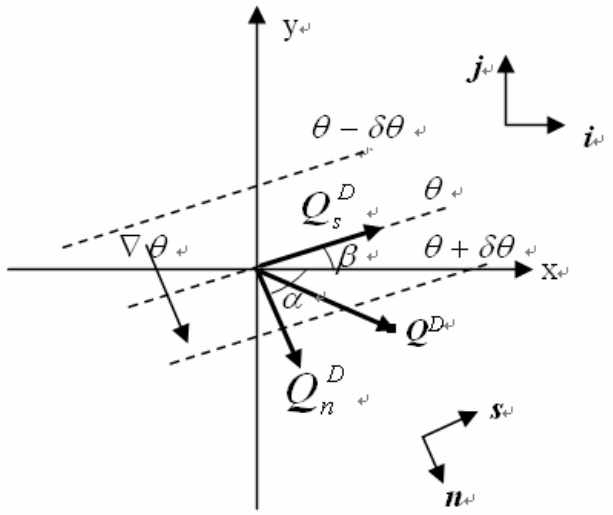

Fig. 7. Schematic diagrams of the partitioning of $\boldsymbol{Q}^D$ vector and Cartesian and natural coordinates. $\boldsymbol{n}$ is a unit vector that points to warm air from cold air, $\boldsymbol{s}$ is a unit vector derived from $\boldsymbol{n}$ rotating 90° counterclockwise. β is an angle between $\boldsymbol{s}$ and the x axis, and α is an angle between $\boldsymbol{n}$ and the x axis, and $\beta+\alpha=90^0$.

In Fig. 7, $\boldsymbol{n}$ is a unit vector along the direction of $\nabla\theta$, and $\boldsymbol{n}=\dfrac{\nabla\theta}{|\nabla\theta|}$. When $\boldsymbol{n}$ rotates 90° counterclockwise, a unit vector $\boldsymbol{s}$ is obtained where $\boldsymbol{s}=\boldsymbol{k}\times\boldsymbol{n}$. $\boldsymbol{Q}_n^D$ denotes the component of dry

ageostrophic $\boldsymbol{Q}$ vector along the direction of $\boldsymbol{n}$, and $\boldsymbol{Q}_n^D = (\frac{\boldsymbol{Q}^D \cdot \nabla\theta}{|\nabla\theta|})\frac{\nabla\theta}{|\nabla\theta|}$ or $\boldsymbol{Q}_n^D = (\frac{\boldsymbol{Q}^D \cdot \nabla\theta}{|\nabla\theta|})\boldsymbol{n}$. $\boldsymbol{Q}_s^D$ denotes the component of dry ageostrophic $\boldsymbol{Q}$ vector along the direction of $\boldsymbol{s}$, and $\boldsymbol{Q}_s^D = \frac{\boldsymbol{Q}^D \cdot (\boldsymbol{k}\times\nabla\theta)}{|\nabla\theta|}[\frac{(\boldsymbol{k}\times\nabla\theta)}{|\nabla\theta|}]$.

$\boldsymbol{Q}_n^D$ and $\boldsymbol{Q}_s^D$ have similar diagnostic features to $\boldsymbol{Q}^D$, and can be expressed in the p-coordinate as

$$\boldsymbol{Q}_n^D = [\frac{(\frac{\partial\theta}{\partial x}Q_x^D + \frac{\partial\theta}{\partial y}Q_y^D)\frac{\partial\theta}{\partial x}}{(\frac{\partial\theta}{\partial x})^2 + (\frac{\partial\theta}{\partial y})^2}]\boldsymbol{i} + [\frac{(\frac{\partial\theta}{\partial x}Q_x^D + \frac{\partial\theta}{\partial y}Q_y^D)\frac{\partial\theta}{\partial y}}{(\frac{\partial\theta}{\partial x})^2 + (\frac{\partial\theta}{\partial y})^2}]\boldsymbol{j} \quad (5)$$

$$\boldsymbol{Q}_s^D = [\frac{(\frac{\partial\theta}{\partial y}Q_x^D - \frac{\partial\theta}{\partial x}Q_y^D)\frac{\partial\theta}{\partial y}}{(\frac{\partial\theta}{\partial x})^2 + (\frac{\partial\theta}{\partial y})^2}]\boldsymbol{i} + [\frac{(-\frac{\partial\theta}{\partial y}Q_x^D + \frac{\partial\theta}{\partial x}Q_y^D)\frac{\partial\theta}{\partial x}}{(\frac{\partial\theta}{\partial x})^2 + (\frac{\partial\theta}{\partial y})^2}]\boldsymbol{j} \quad (6)$$

The derivations of Eqs. (5) and (6) can be found in the appendix. $2\nabla\cdot\boldsymbol{Q}_n^D$ and $2\nabla\cdot\boldsymbol{Q}_s^D$ will be calculated to study the effect of different scale forcing on the development of the torrential rainfall in the following discussions.

In the upper troposphere, the divergence of $2\nabla\cdot\boldsymbol{Q}_n^D$ and convergence of $2\nabla\cdot\boldsymbol{Q}_s^D$ occurred over the area at 2000 BST 24 August (Fig. 8). Both $2\nabla\cdot\boldsymbol{Q}_n^D$ and $2\nabla\cdot\boldsymbol{Q}_s^D$ converged at 0200 BST 25 August while the latter was stronger than the former. During 0800 BST–1400 BST 25 August, $2\nabla\cdot\boldsymbol{Q}_n^D$ became divergent. These indicate that the forcing of $2\nabla\cdot\boldsymbol{Q}_s^D$ favors the development of the torrential rainfall, in particular, $2\nabla\cdot\boldsymbol{Q}_n^D$ forced upward motions at 0200 BST 25 August. The distributions of $2\nabla\cdot\boldsymbol{Q}_n^D$ and $2\nabla\cdot\boldsymbol{Q}_s^D$ in the lower troposphere (not shown) coincide with those in the upper troposphere. This suggests that the large-scale forcing plays an important role in developing torrential rainfall whereas the mesoscale forcing accelerates and intensifies the rainfall.

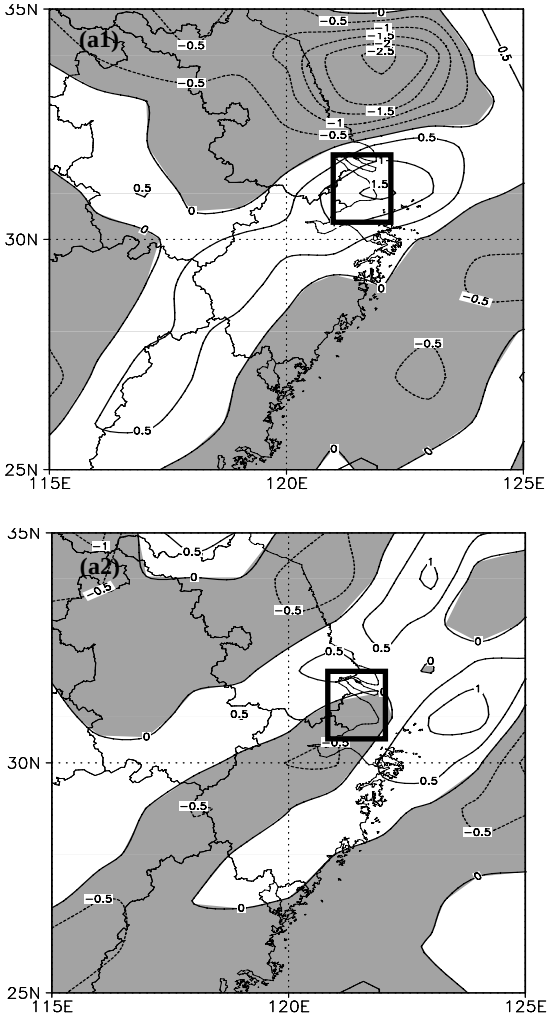

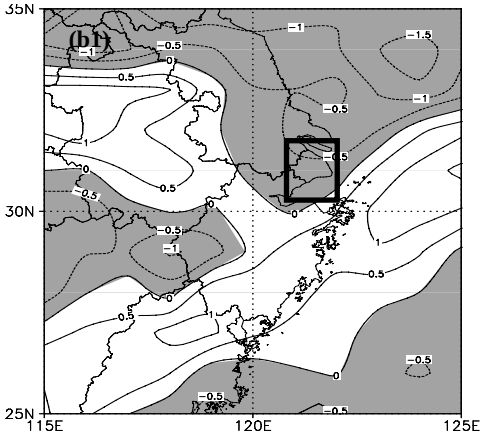

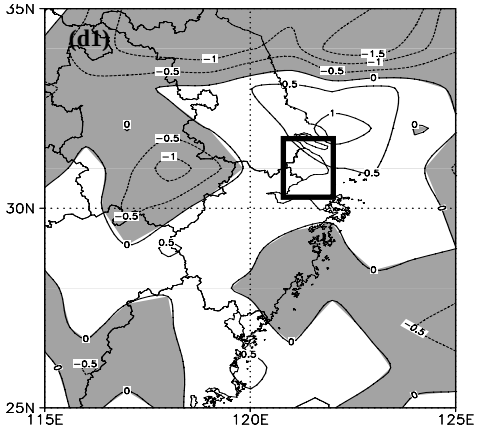

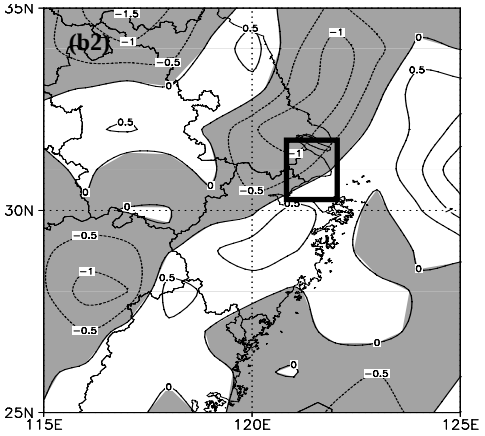

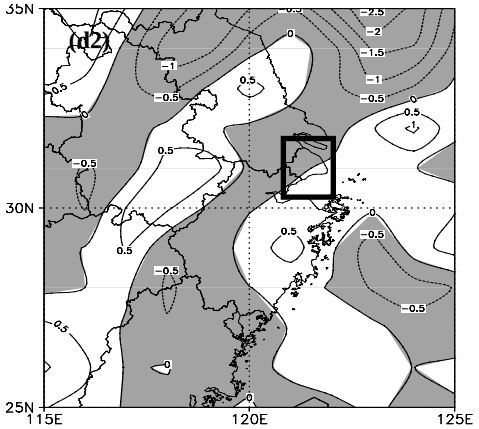

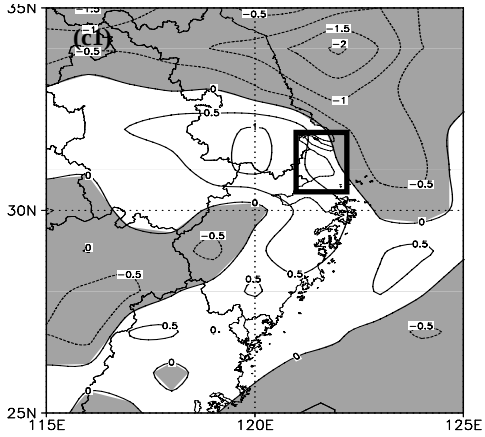

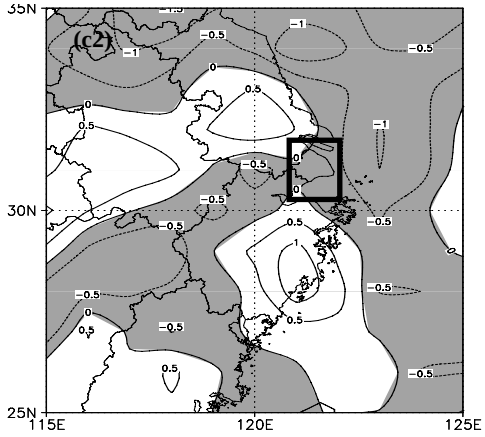

Fig. 8. $2\nabla\cdot\boldsymbol{Q}_n^D$ (a1–d1) and $2\nabla\cdot\boldsymbol{Q}_s^D$ (a2–d2) at (a1) and (a2) 2000 BST 24 August, (b1) and (b2) 0200 BST 25 August, (c1) and (c2) 0800 BST, and (d1) and (d2) 1400 BST 25 August. The contour interval is $0.5\times10^{-15}\,\mathrm{hPa}^{-1}\cdot\mathrm{s}^{-3}$, and the convergence zone is shaded. Shanghai is markded by □.

3.2 *Analysis of diabatic heating*

The aforementioned analysis indicates that plenty of water vapor was available over the area during the development of the torrential rainfall. Thus, the effects of diabatic heating are discussed. From ω equation with the forcing of divergence of moist $\boldsymbol{Q}$ vector, we have

$$\frac{R_d}{C_p\cdot p}\nabla^2(H)\propto\omega_H \tag{7}$$

where H is the diabatic heating rate, ω_H is the vertical velocity forced by diabatic heating in the *p*-coordinate, and the others are conventional meteorological variables and parameters. Eq. (7) has similar diagnostic features to Eq. (4), which is consistent with the results from Long et al.[44] The Laplacian term of diabatic heating in the air column from 1000–100 hPa is calculated to study the role diabatic heating plays in producing vertical motions in the following discussions.

3.2.1 CONDENSATIONAL HEATING H_s^* IN NON-UNIFORM SATURATED ATMOSPHERE

It is not saturated everywhere in the atmosphere. Usually, large relative humidity easily leads to condensation. To solve discontinuation in the transition between saturation and non-saturation areas, Yang et al.[20] and Gao[21] derived a formulation for calculating condensational heating in a non-uniformly saturated atmosphere.

$$H_s^* = -L\frac{d}{dt}[(q_s(\frac{q}{q_s})^k)] \approx -Lq_s(\frac{q}{q_s})^k[\omega(\frac{k}{q}\frac{\partial q}{\partial p}+\frac{1-k}{q_s}\frac{\partial q_s}{\partial p})] \tag{8}$$

where u and v are zonal and meridional components of winds, respectively; ω is the vertical velocity in the p-coordinate, which is obtained with iterative calculation of Eq. (3); q and q_s are specific humidity and saturation specific humidity, respectively, L is the vapor latent heat, and k=9.

In the saturated atmosphere, $q = q_s$, $(\frac{q}{q_s})^k = 1$, Eq. (8) is exactly the same as traditional calculation of condensational heating in the saturated atmosphere. In the non-saturated atmosphere, $0 < q < q_s$, $0 < \frac{q}{q_s} < 1$, Eq. (8) is the function of q and q_s. Thus, H_s^* includes condensational heating and relative humidity, which can be used to study the effects of condensational heating over a transitional zone between the saturated and non-saturated atmosphere on the development of vertical velocity.

Figure 9 shows that $\frac{R_d}{C_p \cdot p}\nabla_h^2(H_s^*)$ was negative over the central and northern areas of Shanghai at 2000 BST 24 August. At 0200 BST 25 August, a negative zone was located in these areas. The negative values covered most of Shanghai during 0800–1400 BST 25 August. Thus, $\frac{R_d}{C_p \cdot p}\nabla_h^2(H_s^*)$ is negative over parts of the area during the development of the torrential rainfall. This implies that the latent heat release is associated with its formation and development, and its positive feedback forces upward motions, which favors the development of the torrential rainfall.

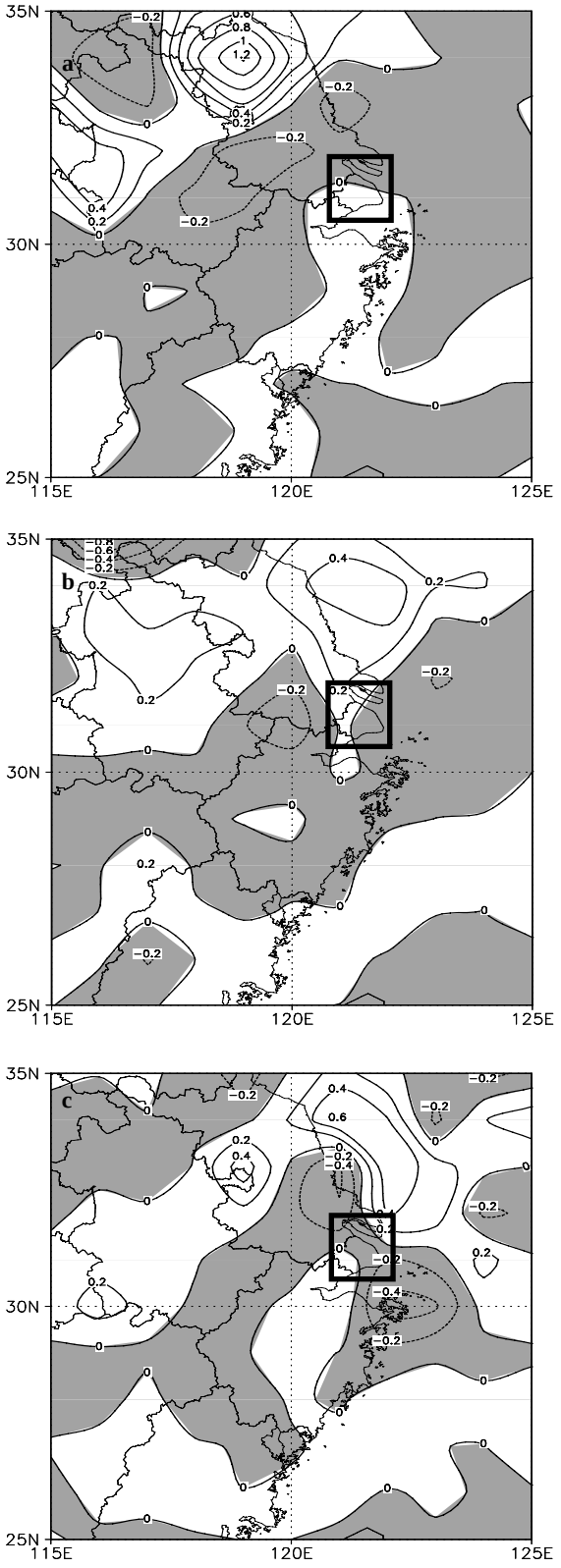

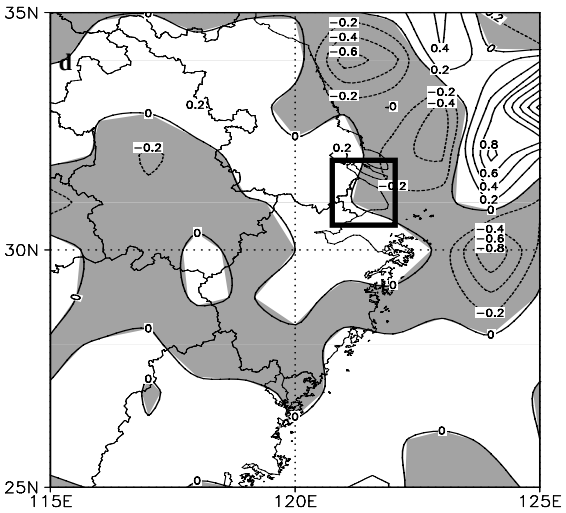

Fig. 9. $\frac{R_d}{C_p \cdot p}\nabla_h^2(H_s^*)$ averaged in air column from 1000–100 hPa at (a) 2000 BST 24 August, (b) 0200 BST 25 August, (c) 0800 BST, and (d) 1400 BST 25 August. The contour interval is $0.2\times10^{-15}\,\mathrm{hPa^{-1}\cdot s^{-3}}$, and negative values are shaded. Shanghai is marked by □.

3.2.2 CONVECTIVE CONDENSATIONAL HEATING H_c

Although H_s^* contains condensational heating over the transitional zone between the saturated and non-saturated atmosphere, it does not include the convective condensational heating. The cumulus parameterization scheme proposed by Kuo[45] is used to calculate the rate of convective condensational heating in this study.

$$H_c = C_p \Delta T . \tag{9}$$

Here $\Delta T = \dfrac{gLI(T_s - T)\pi}{C_p(p_{_B} - p_{_T}) < T_s - T > \tau}$,

where $\pi = \dfrac{\theta}{T} = (\dfrac{1000}{p})^{R_d / C_p}$,

$I = [-\dfrac{1}{g}\int_0^{p_s} (\nabla \cdot q\boldsymbol{V})dp + \rho_s C_d |\boldsymbol{V}_s|(q_s - q)]\tau$,

$< T_s - T >= \dfrac{1}{p_{_B} - p_{_T}} \int_{P_T}^{P_B} (T_s - T)dp$, $p_{_T}$ and $p_{_B}$ are the cloud-top (200 hPa) and cloud-bottom (900 hPa) pressure, respectively, τ is the time scale (30 min.) for cumulus, T_s is the cloud temperature, T is the environmental temperature; p_s, ρ_s, $\boldsymbol{V}_s$ are surface pressure, density, and wind vector, respectively; q_s is the saturated specific humidity over the ocean surface, q is specific humidity near the surface, $C_d = 2.5\times10^{-3}$ is the drag coefficient.

Figure 10 reveals that $\frac{R_d}{C_p \cdot p}\nabla_h^2(H_c)$ was negative over the area at 2000 BST 24 August. The negative values only covered central and northern Shanghai at 0200 BST 25 August. At 0800 BST 25 August, a negative center appeared over the Bay of Hangzhou while the southern Shanghai area had negative values. At 1400 BST 25 August, $\frac{R_d}{C_p \cdot p}\nabla_h^2(H_c)$ became positive over the entire Shanghai area. Before 0800 BST 25 August, convective condensational heating forced upward motions over the area, which favored the development of the torrential rainfall. After that, the positive feedback vanished.

3.2.3 OTHER DIABATIC HEATING Q_d

Diabatic heating includes condensational heating (large-scale, convective components), radiative and sensible heating. The scheme proposed by Gao[21] is used to calculate the diabatic heating $\mathrm{Q_d}$ (excluding condensational heating).

$$\mathrm{Q_d} = \frac{\theta}{\theta^*}\frac{d\theta^*}{dt} \tag{10}$$

Here, $\theta^* = \theta \exp[\dfrac{Lq_s}{C_p T}(\dfrac{q}{q_s})^k]$, which is generalized potential temperature[21], and θ is potential temperature.

$\frac{R_d}{C_p \cdot p}\nabla_h^2(\mathrm{Q_d})$ was negative over most of the area at 2000 BST 24 August (Fig. 10). A negative center of $-2\times10^{-15}\,\mathrm{hPa^{-1}\cdot s^{-3}}$ appeared at 0200 BST 25 August. At 0800 BST, only the northern and southern parts of the area had negative values. Only northern Shanghai had negative values at 1400 BST. This suggests that the negative $\frac{R_d}{C_p \cdot p}\nabla_h^2(\mathrm{Q_d})$ was associated with the development of the torrential rainfall. The diabatic heating has positive feedback to the development of convective systems.

4 DISCUSSIONS

4.1 *Separation of* ***Q*** *vector*

The ***Q*** vector denotes atmospheric dynamic and thermodynamic forcing whereas its separation describes forcing from different physical processes. Both have been widely applied to meteorological studies. Due to the inclusion of diabatic heating, the moist ***Q*** vector is more advanced than the dry

ageostrophic ***Q*** vector. The moist ***Q*** vector is not used in this study. Instead, the components of the dry ***Q*** vector and diabatic heating partitioned from the moist ***Q*** vector are analyzed in this study. Similar to Long et al.[44], such separation is to clearly identify the roles of atmospheric dynamic and thermodynamic forcing and diabatic-heating forcing play in the formation and development of the torrential rainfall. The dry ***Q*** vector is further partitioned along isothermal lines in the natural coordinate to study the effects from different scale forcing, and diabatic heating is further partitioned to identify the effects of large-scale condensational heating in the non-uniform saturated atmosphere, convective condensational heating, and other diabatic heating (including radiative and sensible heating) on rainfall development. Another reason why the moist ***Q*** vector is not directly used for diagnosis is that the forcing from diabatic heating (Figs. 10 & 11) is usually 1–2 orders of magnitude larger than the forcing from the dry ***Q*** vector (Figs. 5 and 6), which is consistent with the results from Yang et al.[20] Although the forcing from the dry ***Q*** vector is relatively small, it is important in predicting the development of the torrential rainfall. Thus, different analysis of the ***Q*** vector can be applied to different scientific issues.

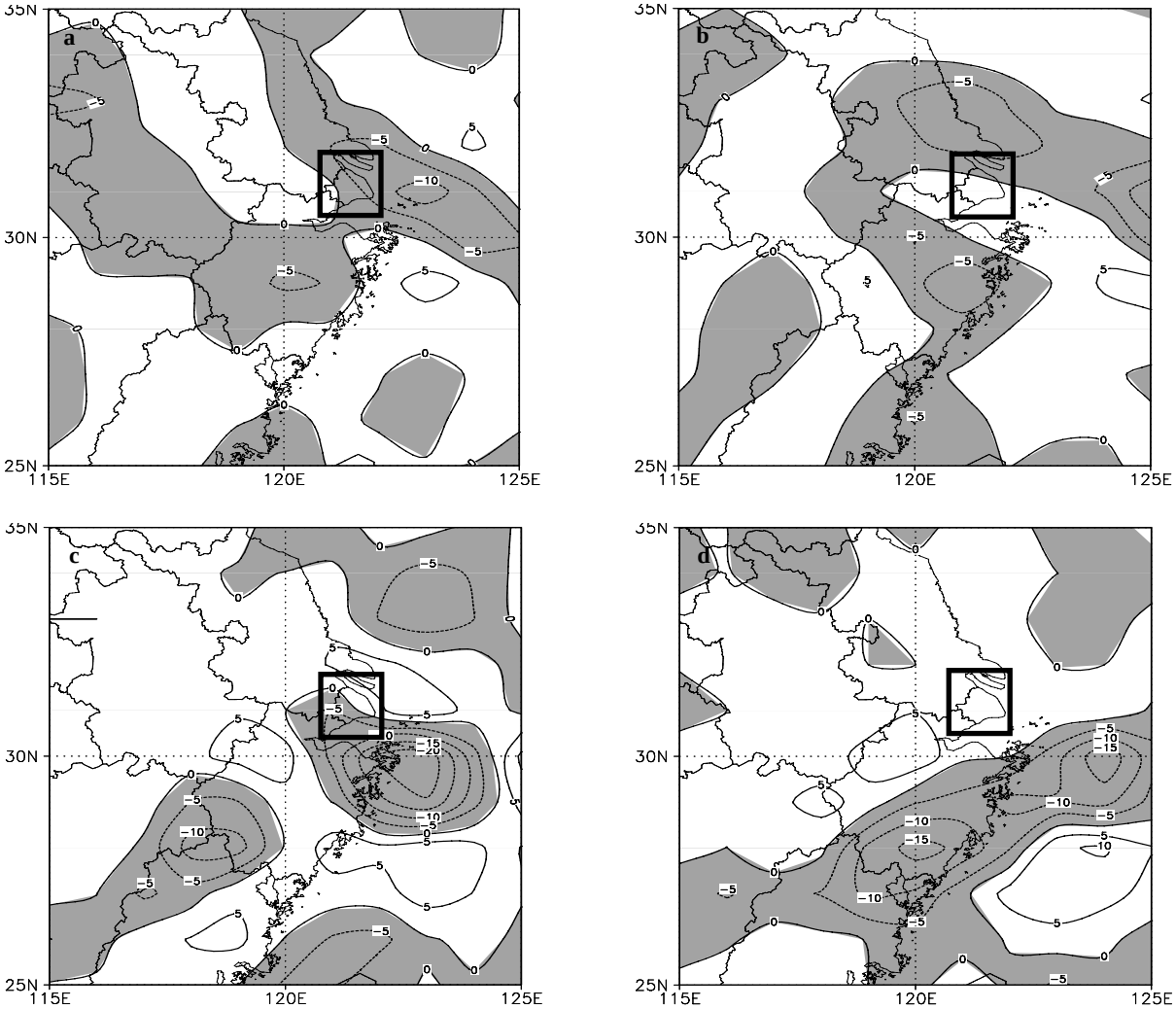

Fig. 10. $\frac{R_d}{C_p \cdot p}\nabla_h^2(H_c)$ averaged in air column from 1000–100 hPa at (a) 2000 BST 24 August, (b) 0200 BST 25 August, (c) 0800 BST, and (d) 1400 BST 25 August. The contour interval is $5\times10^{-15}\,\mathrm{hPa^{-1}\cdot s^{-3}}$, and negative values are shaded. Shanghai is marked by □.

4.2 *Impacts of vertical velocity on calculations of diabatic-heating forcing*

The moist ***Q*** vector explicitly contains diabatic effects. The vertical velocity is needed to calculate the vertical advection term in diabatic effects. The forcing of the ω equation includes vertical velocity, which is problematic as discussed by Yue et al.[3]. Recently, this issue has been intensively addressed and various schemes have been provided to solve this problem. Yue et al.[17, 38, 39] and Yang et al.[20] used outputs of vertical velocity from numerical model simulations. Yue and Shou[19] and Yue[43] used vertical velocity

forced by the dry ageostrophic ***Q*** vector in the calculations of the moist ***Q*** vector. The main idea in previous studies is to assume that the vertical velocities in two sides of the ω equation are different. The vertical velocity included in the forcing of the ω equation is calculated from other sources, which was previously proposed by Ding[46] and Dong and Tian[47]. Thus, different schemes to provide the vertical velocity in the forcing of the ω equation could lead to differences in diabatic effects and the solution of the ω equation. Ding[48] and Gao and Pedder.[49] proposed that the vertical velocities in both sides of the ω equation are the same and moved the forcing term that includes vertical velocity to the left-hand side of the ω equation to solve it. The derived vertical velocity can be used in calculations of the moist ***Q*** vector, avoiding differences in diabatic effects caused by the different schemes of computing vertical velocity. Until now, the explicit calculation of diabatic-heating forcing with vertical velocity has been used in various previous studies. The implicit schemes need further studies.

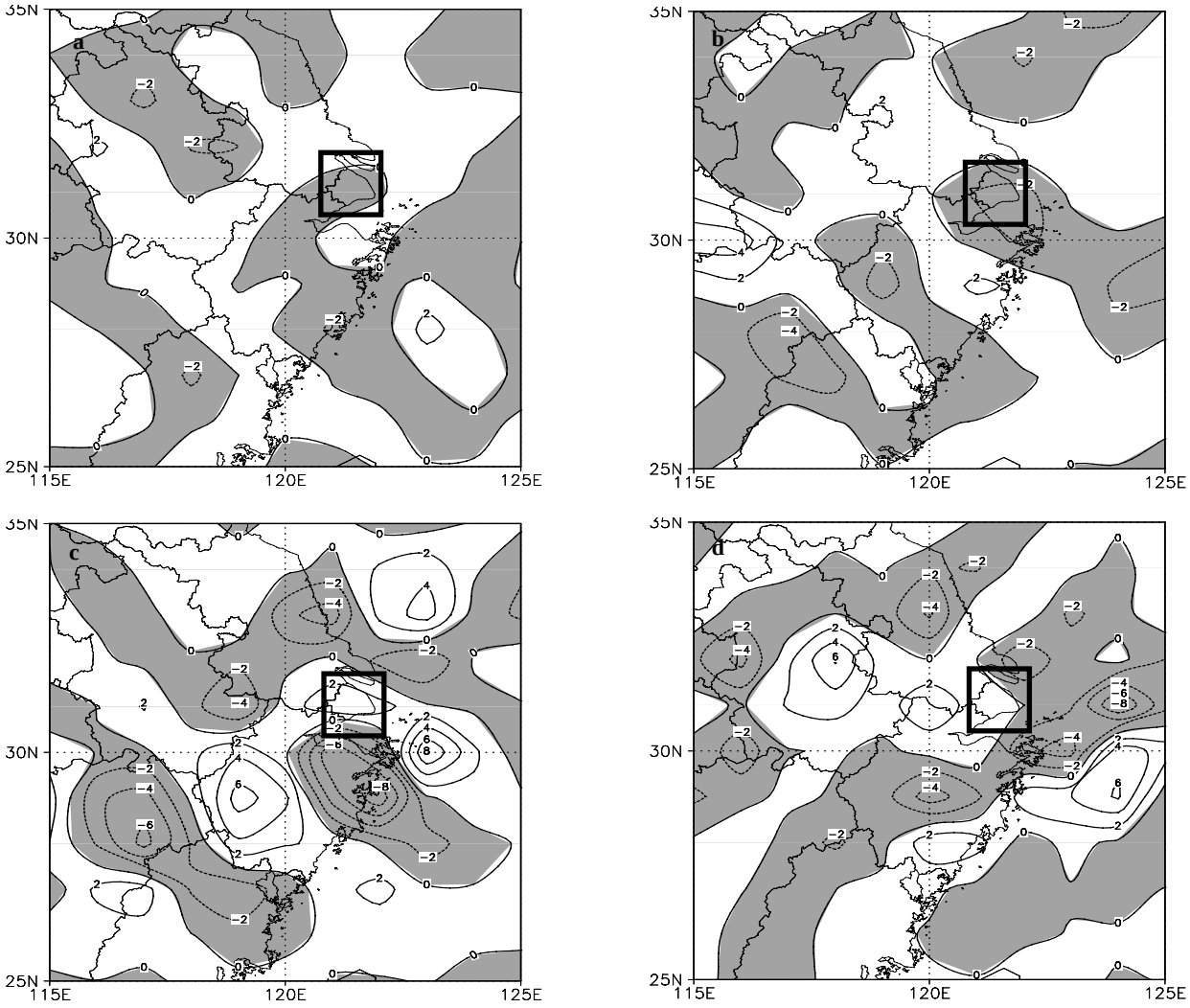

Fig. 11. $\frac{R_d}{C_p \cdot p}\nabla_h^2(\mathrm{Q_d})$ averaged in air column from 1000–100 hPa at (a) 2000 BST 24 August, (b) 0200 BST 25 August, (c) 0800 BST, and (d) 1400 BST 25 August. The contour interval is $2\times10^{-15}\,\mathrm{hPa^{-1}\cdot s^{-3}}$, and negative values are shaded. □ denotes Shanghai's position.

4.3 *Role of backgrounds*

Section 3.1.1 shows that the development of the torrential rainfall is associated with the convergence of the dry ageostrophic ***Q*** vector. The torrential rainfall reaches its peak when the ***Q*** vector switches from convergence to divergence. The rainfall dissipates as the divergence of ***Q*** vector dominates. The convergence of ***Q*** vector is significantly stronger in the upper troposphere than in the lower troposphere, indicating the important roles the upper troposphere plays in forcing vertical velocity. Section 2.3 shows that the eastward propagation of a westerly low-pressure trough at 500 hPa is closely associated with a low vortex at 850 hPa. Based on the results from Shou et al.[50], the formation of a low vortex in

the lower troposphere at 0200 BST 25 August resulted from downward propagation of high energy in the upper troposphere. Section 3.1.2 reveals that lower-tropospheric dynamic and thermodynamic forcing in the dry, adiabatic atmosphere and large-scale forcing in the entire air column favor the development of the torrential rainfall. Section 3.2 shows that the adiabatic heating has the positive feedback to the development of convective systems. Based on the findings above, environmental conditions are conducive to the development of rainfall processes, specifically, dynamic and thermodynamic forcing in lower-tropospheric dry and adiabatic atmosphere and tropospheric large-scale forcing are almost always favorable for the development of the torrential rainfall. The energy in the upper-tropospheric dry and adiabatic atmosphere increases and propagates downward and tropospheric mesoscale forcing occurs, accelerating the development of rainfall. The positive feedback of diabatic heating also sets favorable conditions for the development of torrential rainfall. All of the active roles of background above decay and dissipate along with the convective system propagating eastward and weakening.

5 CONCLUSIONS

The analysis of partitioning of the ***Q*** vector is carried out in this study with NCEP/NCAR FNL data to diagnose backgrounds associated with a torrential rainfall event that occurred from 0200–1400 BST 25 August 2008. The results include the followings.

(1) A low-pressure inverted trough associated with the landfall of Typhoon Nuri (2008), a strong southwesterly jet along the western side of the subtropical high, and an eastward-propagating westerly low-pressure trough provide favorable synoptic conditions for the development of the torrential rainfall.

(2) The analysis of the dry ageostrophic ***Q*** vector reveals that the lower-tropospheric forcing favors the development of the torrential rainfall whereas the downward propagation of high energy in the upper troposphere accelerates the development of the torrential rainfall. The evolution of convergence of the dry ageostrophic ***Q*** vector in the entire air column is an excellent precursor for the intensity of the torrential rainfall. Large-scale forcing favors the formation and development of the torrential rainfall whereas mesoscale forcing accelerates its development.

(3) The calculations of Laplacian terms of various diabatic effects show that the upward motions forced by various diabatic effects have positive feedbacks on the development of the torrential rainfall.

Note that only coarse resolution data are used to diagnose the environmental conditions in this study, which cannot meet the need of direct analysis of the internal cause of the torrential rainfall. Finer temporal and spatial resolution data are needed for further studying physical mechanisms associated with the formation and development of torrential rainfall.

***Acknowledgement*:** The authors thank anonymous reviewers for their valuable comments and SHI Chun-hong and DAI Jian-hua, Principal Forecasters, Shanghai Meteorological Center for their help.

REFERENCES:

[1] CAO Xiao-gang, ZHANG Ji, WANG Hui, et al. Analysis on a severe convective rainstorm hitting Shanghai on 25 August 2008 [J]. Meteor. Mon., 2009, 25: 51-58.

[2] YUE Cai-jun. The advances on the ***Q*** vector and its application to synoptic diagnosis [J]. Meteor. Mon., 1999, 25: 3-8.

[3] YUE Cai-jun, SHOU Yi-xuan, SHOU Shao-wen, et al. Application and research on ***Q***-vector analytic method in China [J]. Plateau Meteor., 2005, 24: 450-455.

[4] YUE Cai-jun, SHOU Shao-wen, YAO Xiu-ping. Recent advances on application study of ***Q*** vector to diagnostic analysis and prediction of severe weathers [J]. J. Trop. Meteor., 2008, 24: 557-563.

[5] HOSKINS B J, DAGBICI I, DARICS H C. A new look at the ω -equation [J]. Quart. J. Roy. Meteor. Soc., 1978, 104(439): 31-38.

[6] LI Bai, LI Guo-jie. Application of the semi-geostrophic ***Q*** vector in study of the Meiyu front heavy rain [J]. Atmos. Sci. Res. Appl., 1997, 12: 31-38.

[7] DAVIES J R. The frontogenetical forcing of secondary circulations, Part I: the duality and generalization of the ***Q*** vector [J]. J. Atmos. Sci., 1991, 48(4): 497-509.

[8] XU Q. Ageostrophic pseudovorticity and geostrophic ***C***-vector forcing—a new look at ***Q*** vector in three dimensions [J]. J. Atmos. Sci., 1992, 49: 981-990.

[9] MIAO Jin-hai. The generalized ***C*** vector and meso-scale circulation [C]// Scientific and Operational Experiments on Heavy Rainfall and Study on Theory of Synaptic Dynamics (Grant No. 85-906-08), Beijing: China Meteorological Press, 1996, 235-237.

[10] ZHANG Xing-wang. The expression of the modified ***Q*** vector and its application [J]. J. Trop. Meteor., 1999, 15: 162-167.

[11] YUE Cai-jun. The ***Q*** vector analysis of the heavy rainfall from Meiyu Front cyclone: A case study [J]. Acta Meteor. Sinica, 2008, 66: 35-49.

[12] YUE Cai-jun. ***Q*** vector partitioning study on effects of typhoon structures on precipitation associated with typhoon Haitang (2005) [J]. Plateau Meteor., 2009, 28(6): 1348-1364.

[13] ZHANG Xing-wang. An expression of the wet ***Q*** vector and application [J]. Meteor. Mon., 1998, 24: 3-7.

[14] YAO Xiu-ping, YU Yu-bin. Non-geostrophic wet ***Q***-vector analysis and its application to typhoon torrential rain [J]. Acta Meteor. Sin., 2000, 58: 436-446.

[15] YAO Xiu-ping, YU Yu-bin. Perfect ***Q***-vector and its diagnoses [J]. Plateau Meteor., 2001, 20: 208-213.

[16] YAO Xiu-ping, YU Yu-bin, SHOU Shao-wen. Diagnostic analyes and application of the moist ageostrophic ***Q*** vector [J]. Adv. Atmos. Sci., 2004, 21: 96-102.

[17] YUE Cai-jun, SHOU Yi-xuan, SHOU Shao-wen, et al. The

improvement and perfection of ***Q*** vector [J]. J. Trop. Meteor., 2003, 19: 308-316.
[18] LIU Han-hua, SHOU Shao-wen, ZHOU Jun. Improvement and application of ageostrophic wet ***Q***-vector [J]. J. Nanjing Inst. Meteor., 2007, 30: 86-93.
[19] YUE Cai-jun, SHOU Shao-wen. A modified moist ageostrophic ***Q*** vector [J]. Adv. Atmos. Sci., 2008, 25: 1053-1061.
[20] YANG S, GAO S, WANG D. Diagnostic analyses of the ageostrophic $\vec{Q}$ vector in the non-uniformly saturated, frictionless, and moist adiabatic flow [J]. J. Geophys. Res., 2007, 112 (D09114): 1-9, doi: 10.1029/2006JD008142.
[21] GAO Shou-ting. Dynamical Basis and Forecast Methods of Atmospheric Meso-scale Motion [M]. Beijing: China Meteorological Press, 2007, 191-200.
[22] KEYSER D, REEDER M J, REED R J. A generalization of Petterssen's frontogenesis function and its relation to the forcing of vertical motion [J]. Mon. Wea. Rev., 1988, 116: 762-780.
[23] KEYSER D, SCHMIDT B D, DUFFY D G. Quasi-geostrophic vertical motions diagnosed from along- and cross-isentrope components of the ***Q*** vector [J]. Mon. Wea. Rev., 1992, 20: 731-741.
[24] KURZ M. Synoptic diagnosis of frontogenetic and cyclogenetic processes [J]. Meteor. Atmos. Phys., 1992, 48: 77-91.
[25] KURZ M. The role of frontogenetic and frontolytic wind field effects during cyclonic development [J]. Meteor. Appl., 1997, 4: 353-363.
[26] BARNES S L, COLMAN B R. Quasigeostrophic diagnosis of cyclogenesis associated with a cut off extratropical cyclone - The Christmas 1987 storm [J]. Mon. Wea. Rev., 1993, 121: 1613-1634.
[27] BARNES S L, COLMAN B R. Diagnosing an operational numerical model using ***Q***-vector and potential vorticity concepts [J]. Wea. And Forecasting, 1994, 9: 85-102.
[28] SCHAR C, WERNLI H. Structure and evolution of an isolated semi-geostrophic cyclone [J]. Quart. J. Roy. Meteor. Soc., 1993, 119: 57-90.
[29] MARTIN J E. Quasi-geostrophic forcing of ascent in the occluded sector of cyclones and the trowal airstream [J]. Mon. Wea. Rev., 1999, 127: 70-88.
[30] PYLE M E, KEYSER D, BOSART L F. A diagnostic study of jet streaks: Kinematic signatures and relationship to coherent tropopause disturbances [J]. Mon. Wea. Rev., 2004, 132: 297-319.
[31] MARTIN J E. The role of shearwise and transverse quasigeostrophic vertical motions in the midlatitude cyclone life cycle [J]. Mon. Wea. Rev., 2006, 134: 1174-1193.
[32] MARTIN J E. Lower-tropospheric height tendencies associated with the shearwise and transverse components of quasigeostrpphic vertical motion [J]. Mon. Wea. Rev., 2007, 135: 2 803-2 809.
[33] THOMAS B C, MARTIN J E. A synoptic climatology and composite analysis of the Alberta Clipper [J]. Wea. Forecasting, 2007, 22: 315-333.
[34] JUSEM J C, ATLAS R. Diagnostic evaluation of vertical motion forcing mechanism by using ***Q***-vector partitioning [J]. Mon. Wea. Rev., 1998, 126(8): 2166-2184.
[35] DONNADILLE J, CAMMAS J P, MASCART P, et al. FASTEX IOP 18: a very deep tropopause fold. II: quasi-geostrophic omega diagnoses [J]. Quart. J. Roy. Meteor. Soc., 2001, 127: 2269-2286.
[36] MARTIN J E. The separate roles of geostrophic vorticity and deformation in the midlatitude occlusion process [J]. Mon. Wea. Rev., 1999, 127: 2404-2418.
[37] MORGAN M C. Using piecewise potential vorticity inversion to diagnose frontogenesis. Part I: a partitioning of the ***Q*** vector applied to diagnosing surface frontogenesis and vertical motion [J]. Mon. Wea. Rev., 1999, 127: 2796-2821.
[38] YUE Cai-jun, SHOU Shao-wen, LIN Kai-ping, et al. Diagnosis of the heavy rain near a Meiyu front using the wet ***Q*** vector partitioning method [J]. Adv. Atmos. Sci., 2003, 20: 37-44.
[39] YUE Cai-jun, DONG Mei-ying, SHOU Shao-wen, et al. Improved wet ***Q*** vector's analytical method and the mechanism of Meiyu front rainstorm genesis [J]. Plateau Meteor., 2007, 26: 165-175.
[40] WANG Chuan, DU Chuan-li, SHOU Shao-wen. Application of ***Q***-vector theory to "02.6" heavy storm rain on the east side of Qinghai-Xizhang Plateau [J]. Plateau Meteor., 2005, 24(2): 261-267.
[41] YANG Xiao-xia, SHEN Tong-li, LIU Huan-zhu, et al. Application of the wet ***Q*** vector partitioning method to the diagnosis of the heavy rainstorm [J]. Plateau Meteor., 2006, 25: 464-475.
[42] LIANG Lin-lin, SHOU Shao-wen, MIAO Chun-sheng. Diagnostic analysis of a Meiyu front heavy rain process in July 2005 using wet ***Q*** vector partitioning theory [J]. J. Nanjing Inst. Meteor., 2008, 31: 167-175.
[43] YUE Cai-jun. Quantitative analysis of torrential rainfall associated with typhoon landfall: A case study of typhoon Haitang (2005) [J]. Prog. Nat. Sci., 2009, 19: 55-63.
[44] LONG Xiao, CHENG Lin-sheng, MEI Chun-jie. Perfect ***Q***-vector and its applications on rainstorms' diagnosis [J]. J. Lanzhou Univ. (Nat. Sci. edition), 2006, 24(3): 32-39.
[45] KUO H L. Further studies of the parameterization of the influence of cumulus convection on large-scale flow [J]. J. Atmos. Sci., 1974, 31: 1232-1240.
[46] DING De-gang. Calculation of Vertical Velocity in Atmosphere [M]. Beijing: China Meteorological Press, 1985, 19-23.
[47] DONG Xiao-min, TIAN Sheng-pei. Simple Introduction of Synoptic Diagnostic Analysis [M]. Beijing: China Meteorological Press, 1986, 25-37.
[48] DING Yi-hui. Diagnostic and analytical methods in synoptic dynamics [M]. Beijing: Science Press, 1989.
[49] GAO Shao-feng, PEDDER M A. The role released latent heat in vertical motion of the ω –equation [J]. J. Trop. Meteor., 1991, 7(1): 88-93.
[50] SHOU Shao-wen, LI Yao-hui, FAN Ke. Isentropic potential vorticity analysis of the mesoscale cyclone development in a heavy rain process [J]. Acta Meteor. Sinica, 2001, 59: 560-568.

Citation: YUE Cai-jun, LU Xiao-qin, Xiaofan LI et al. A study of partitioning ***Q*** vector on background conditions of a torrential rainfall over Shanghai, China on 25 August 2008. *J. Trop. Meteor.*, 2011, 17(3): 231-247.

Appendix 1 Derivation of $\boldsymbol{Q}_n^D$ and $\boldsymbol{Q}_s^D$ in the *p*-coordinate

In Fig. 7, $\nabla\theta$ points to warm air from cold air, which is opposite to gradient of potential temperature ($-\nabla\theta$). α is an angle between ***n*** and the *x* axis, and ***n*** is a unit vector that points to warm air from cold air along $\nabla\theta$. Thus, α is an angle between $\nabla\theta$ and *x* axis. $\nabla\theta$ can be expressed by

$$\nabla\theta = (\nabla\theta \cdot \boldsymbol{i})\boldsymbol{i} + (\nabla\theta \cdot \boldsymbol{j})(-\boldsymbol{j}), \quad \text{(A0)}$$

where $\boldsymbol{i}$ and $\boldsymbol{j}$ are, respectively, unit vectors along the x and y axis, i.e., $|\boldsymbol{i}|=1$, $|\boldsymbol{j}|=1$, and the magnitude of $\nabla\theta$ is $|\nabla\theta|$. (A0) becomes

$$\nabla\theta = (|\nabla\theta|\cos\alpha)\boldsymbol{i} + (|\nabla\theta|\cos(90^0-\alpha))(-\boldsymbol{j}) \quad \text{(A1)}$$

Since $\beta+\alpha=90^0$, $\alpha=90^0-\beta$. (A1) becomes

$$\nabla\theta = |\nabla\theta|\cos(90^0-\beta)\boldsymbol{i} + (|\nabla\theta|\cos\beta)(-\boldsymbol{j}) \quad \text{(A2)}$$

And (A2) can be in turn written as

$$\nabla\theta = (|\nabla\theta|\sin\beta)\boldsymbol{i} + (-|\nabla\theta|\cos\beta)\boldsymbol{j} \quad \text{(A3)}$$

Arrangement of (A3) leads to

$$\nabla\theta = |\nabla\theta|[(\sin\beta)\boldsymbol{i} + (-\cos\beta)\boldsymbol{j}] \quad \text{(A4)}$$

Because

$$\nabla\theta = \frac{\partial\theta}{\partial x}\boldsymbol{i} + \frac{\partial\theta}{\partial y}\boldsymbol{j} \quad . \quad \text{(A5)}$$

From (A4) and (A5), we get

$$\frac{\partial\theta}{\partial x} = |\nabla\theta|\sin\beta, \quad \frac{\partial\theta}{\partial y} = -|\nabla\theta|\cos\beta,$$

$$\text{or} \quad \sin\beta = \frac{\dfrac{\partial\theta}{\partial x}}{|\nabla\theta|}, \quad \cos\beta = \frac{-\dfrac{\partial\theta}{\partial y}}{|\nabla\theta|}.$$

Since $\boldsymbol{n}$ is along $\nabla\theta$, from (A0) - (A3), we get

$$\boldsymbol{n} = (|n|\sin\beta)\boldsymbol{i} + (-|n|\cos\beta)\boldsymbol{j}. \quad \text{(A6)}$$

Because $\boldsymbol{n}$ is the unit vector, i.e., $|\boldsymbol{n}|=1$, (A6) becomes

$$\boldsymbol{n} = (\sin\beta)\boldsymbol{i} + (-\cos\beta)\boldsymbol{j} \quad \text{(A7)}$$

Substituting $\sin\beta = \dfrac{\dfrac{\partial\theta}{\partial x}}{|\nabla\theta|}$ and $\cos\beta = \dfrac{-\dfrac{\partial\theta}{\partial y}}{|\nabla\theta|}$ into (A7) yields

$$\boldsymbol{n} = \frac{\dfrac{\partial\theta}{\partial x}\boldsymbol{i}}{|\nabla\theta|} + \frac{\dfrac{\partial\theta}{\partial y}\boldsymbol{j}}{|\nabla\theta|} \quad . \quad \text{(A8)}$$

(A8) can be written as

$$\boldsymbol{n} = \frac{\nabla\theta}{|\nabla\theta|}. \quad \text{(A9)}$$

$\boldsymbol{s}$ is a unit vector derived from $\boldsymbol{n}$ rotating 90^o counterclockwise, i.e.,

$$\boldsymbol{s} = \boldsymbol{k}\times\boldsymbol{n} \quad . \quad \text{(A10)}$$

Substituting (A9) into (A10) leads to

$$\boldsymbol{s} = \frac{\boldsymbol{k}\times\nabla\theta}{|\nabla\theta|} \quad \text{(A11)}$$

Putting (A5) into (A11) generates

$$\boldsymbol{s} = \frac{-\dfrac{\partial\theta}{\partial y}\boldsymbol{i}}{|\nabla\theta|} + \frac{\dfrac{\partial\theta}{\partial x}\boldsymbol{j}}{|\nabla\theta|} \quad \text{(A12)}$$

Figure 7 shows that $\boldsymbol{Q^D}$ can be partitioned into $\boldsymbol{Q}_n^D$ and $\boldsymbol{Q}_s^D$ in the natural coordinate, i.e.,

$$\boldsymbol{Q}^D = \boldsymbol{Q}_n^D + \boldsymbol{Q}_s^D = (\boldsymbol{n}\cdot\boldsymbol{Q}^D)\boldsymbol{n} + (\boldsymbol{s}\cdot\boldsymbol{Q}^D)\boldsymbol{s} \quad \text{(A13)}$$

From (A13), we have

$$\boldsymbol{Q}_n^D = (\boldsymbol{n}\cdot\boldsymbol{Q}^D)\boldsymbol{n} \quad \text{(A14)}$$

$$\boldsymbol{Q}_s^D = (\boldsymbol{s}\cdot\boldsymbol{Q}^D)\boldsymbol{s} \quad \text{(A15)}$$

Also,

$$\boldsymbol{Q}^D = Q_x^D\boldsymbol{i} + Q_y^D\boldsymbol{j} \quad \text{(A16)}$$

Substituting (A8) and (A16) into (A14) produces

$$\boldsymbol{Q}_n^D = \frac{(\dfrac{\partial\theta}{\partial x}\boldsymbol{i} + \dfrac{\partial\theta}{\partial y}\boldsymbol{j})\cdot(Q_x^D\boldsymbol{i} + Q_y^D\boldsymbol{j})}{|\nabla\theta|}\frac{(\dfrac{\partial\theta}{\partial x}\boldsymbol{i} + \dfrac{\partial\theta}{\partial y}\boldsymbol{j})}{|\nabla\theta|} \quad \text{(A17)}$$

Substitution of $|\nabla\theta| = \sqrt{(\dfrac{\partial\theta}{\partial x})^2 + (\dfrac{\partial\theta}{\partial y})^2}$ into (A17) leads to

$$\begin{aligned}\boldsymbol{Q}_n^D &= \frac{(\dfrac{\partial\theta}{\partial x}Q_x^D + \dfrac{\partial\theta}{\partial y}Q_y^D)}{\sqrt{(\dfrac{\partial\theta}{\partial x})^2 + (\dfrac{\partial\theta}{\partial y})^2}}\cdot\frac{(\dfrac{\partial\theta}{\partial x}\boldsymbol{i} + \dfrac{\partial\theta}{\partial y}\boldsymbol{j})}{\sqrt{(\dfrac{\partial\theta}{\partial x})^2 + (\dfrac{\partial\theta}{\partial y})^2}} \\ &= [\frac{(\dfrac{\partial\theta}{\partial x}Q_x^D + \dfrac{\partial\theta}{\partial y}Q_y^D)\dfrac{\partial\theta}{\partial x}}{(\dfrac{\partial\theta}{\partial x})^2 + (\dfrac{\partial\theta}{\partial y})^2}]\boldsymbol{i} \\ &\quad + [\frac{(\dfrac{\partial\theta}{\partial x}Q_x^D + \dfrac{\partial\theta}{\partial y}Q_y^D)\dfrac{\partial\theta}{\partial y}}{(\dfrac{\partial\theta}{\partial x})^2 + (\dfrac{\partial\theta}{\partial y})^2}]\boldsymbol{j}\end{aligned} \quad \text{(A18)}$$

Putting (A12) and (A16) into (A15) yields

$$\boldsymbol{Q}_s^D = \frac{(-\dfrac{\partial\theta}{\partial y}\boldsymbol{i} + \dfrac{\partial\theta}{\partial x}\boldsymbol{j})\cdot(Q_x^D\boldsymbol{i} + Q_y^D\boldsymbol{j})}{|\nabla\theta|}\frac{(-\dfrac{\partial\theta}{\partial y}\boldsymbol{i} + \dfrac{\partial\theta}{\partial x}\boldsymbol{j})}{|\nabla\theta|} \quad \text{(A19)}$$

Substitution of $|\nabla\theta| = \sqrt{(\dfrac{\partial\theta}{\partial x})^2 + (\dfrac{\partial\theta}{\partial y})^2}$ into (A19) generates

$$\begin{aligned}\boldsymbol{Q}_s^D &= \frac{(-\dfrac{\partial\theta}{\partial y}Q_x^D + \dfrac{\partial\theta}{\partial x}Q_y^D)}{\sqrt{(\dfrac{\partial\theta}{\partial x})^2 + (\dfrac{\partial\theta}{\partial y})^2}}\cdot\frac{(-\dfrac{\partial\theta}{\partial y}\boldsymbol{i} + \dfrac{\partial\theta}{\partial x}\boldsymbol{j})}{\sqrt{(\dfrac{\partial\theta}{\partial x})^2 + (\dfrac{\partial\theta}{\partial y})^2}} \\ &= [\frac{(\dfrac{\partial\theta}{\partial y}Q_x^D - \dfrac{\partial\theta}{\partial x}Q_y^D)\dfrac{\partial\theta}{\partial y}}{(\dfrac{\partial\theta}{\partial x})^2 + (\dfrac{\partial\theta}{\partial y})^2}]\boldsymbol{i} \\ &\quad + [\frac{(-\dfrac{\partial\theta}{\partial y}Q_x^D + \dfrac{\partial\theta}{\partial x}Q_y^D)\dfrac{\partial\theta}{\partial x}}{(\dfrac{\partial\theta}{\partial x})^2 + (\dfrac{\partial\theta}{\partial y})^2}]\boldsymbol{j}\end{aligned} \quad \text{(A20)}$$

(A18) and (A20) are, respectively, Eq. (5) and Eq. (6) in the text.